



Whole-body MRI: detecting bone metastases from prostate cancer

Katsuyuki Nakanishi¹ · Junichiro Tanaka¹ · Yasuhiro Nakaya¹ · Noboru Maeda¹ · Atsuhiko Sakamoto¹ · Akiko Nakayama¹ · Hiroki Satomura¹ · Mio Sakai¹ · Koji Konishi² · Yoshiyuki Yamamoto³ · Akira Nagahara³ · Kazuo Nishimura³ · Satoshi Takenaka⁴ · Noriyuki Tomiyama⁵

Received: 31 March 2021 / Accepted: 29 September 2021 / Published online: 25 October 2021
© The Author(s) 2021

Abstract

Whole-body magnetic resonance imaging (WB-MRI) is currently used worldwide for detecting bone metastases from prostate cancer. The 5-year survival rate for prostate cancer is > 95%. However, an increase in survival time may increase the incidence of bone metastasis. Therefore, detecting bone metastases is of great clinical interest. Bone metastases are commonly located in the spine, pelvis, shoulder, and distal femur. Bone metastases from prostate cancer are well-known representatives of osteoblastic metastases. However, other types of bone metastases, such as mixed or inter-trabecular type, have also been detected using MRI. MRI does not involve radiation exposure and has good sensitivity and specificity for detecting bone metastases. WB-MRI has undergone gradual developments since the last century, and in 2004, Takahara et al., developed diffusion-weighted Imaging (DWI) with background body signal suppression (DWIBS). Since then, WB-MRI, including DWI, has continued to play an important role in detecting bone metastases and monitoring therapeutic effects. An imaging protocol that allows complete examination within approximately 30 min has been established. This review focuses on WB-MRI standardization and the automatic calculation of tumor total diffusion volume (tDV) and mean apparent diffusion coefficient (ADC) value. In the future, artificial intelligence (AI) will enable shorter imaging times and easier automatic segmentation.

Keywords Whole-body MRI · Prostate cancer · Bone metastases · DWIBS

Introduction

There are significant advantages to using whole-body magnetic resonance imaging (WB-MRI) for detecting bone metastases. Evaluation can be performed with a single scan, which is potentially more cost-effective and time-saving for whole-body evaluations [1–5]. Moreover, it can be used for whole-body evaluation and treatment response monitoring. In particular, diffusion-weighted imaging (DWI) has become available for whole-body scanning, which has now been incorporated into the main sequence of WB-MRI. Prostate cancer is the most frequent malignant tumor in older men and is associated with a high rate of recurrence [6]. Therefore, the use of WB-MRI has become frequent.

This review article aims to provide a general statement on bone metastases, explain the developmental history of WB-MRI, provide an interpretation of imaging methods with WB-MRI, present the details of some typical cases of bone metastases from prostate cancer, and discuss the future of WB-MRI.

General statement on bone metastases

Bone metastasis is a devastating condition that has wide-ranging negative impacts on the lives of patients with advanced cancer [7]. To date, no large-scale etiological studies on the prevalence or incidence of bone metastasis

✉ Katsuyuki Nakanishi
je2k-nkns@hera.eonet.ne.jp

Extended author information available on the last page of the article

have been conducted worldwide [7]. However, the current 5-year survival rate for prostate cancer is > 95% across numerous countries [8], and an increase in survival time may increase the incidence of bone metastasis.

Irrespective of the primary malignant location, bone metastases are commonly found in the spine, pelvis, shoulder, and distal femur [9, 10]. These bone lesions can cause serious complications, such as spinal cord and nerve root compression, pathological fracture, and hypercalcemia [9]. Bone metastases most commonly affect the axial skeleton. In adults, the axial skeleton contains red marrow, which suggests that the properties of the circulation, cells and extracellular matrix within this region assist in the formation of bone metastasis [10]. Batson [11] showed that venous blood from the breast and pelvis flowed not only into the vena cava but also into the vertebral venous plexus, which extends from the pelvis to throughout the epidural and peri-vertebral veins [11, 12] (Fig. 1). Blood drainage to the skeleton via the vertebral venous plexus may, at least in part, explain the tendency of breast and prostate cancers (as well as those arising in the kidney, thyroid, and lung) to produce metastases in the axial skeleton and limb girdles [10, 11].

Conventional classifications categorize bone metastases as osteoblastic, osteolytic and mixed types [9, 13]. This classification is based on the primary mechanism of interference with normal bone remodeling [13] and the uptake of radiotracers, which depends on the quantity of the calcification of the metastases and osteoblastic activity [9]. However, the recently identified inter-trabecular-type metastasis, which infiltrates the marrow space without altering the trabecular bone and is not radiologically visible but detectable on MRI, requires further characterization [14, 15].

Bone metastases from prostate cancer are a well-established example of osteoblastic metastases [9, 13, 16] (Fig. 2). In prostate cancer, prostate-specific antigen (PSA) inhibits parathyroid hormone-related peptides, which leads to the enhancement of osteoblast function [9, 11, 17]. However, the development of various imaging modalities has enabled the detection of other types of metastases, such as mixed or inter-trabecular types (Fig. 3).

Imaging modalities for diagnosing bone metastases include technetium-99 m bone scintigraphy (BS), plain radiography, computed tomography (CT), MRI, and 18F fluorodeoxyglucose (FDG)-positron emission tomography (PET) [7, 13].

BS is highly sensitive but usually has low specificity [13]. It is more sensitive than plain film and CT scans; however, MRI is superior for the evaluation of vertebral metastases [18]. BS provides information on osteoblastic activity and skeletal vascularity with preferential uptake of tracers at sites with active bone formation, which reflects

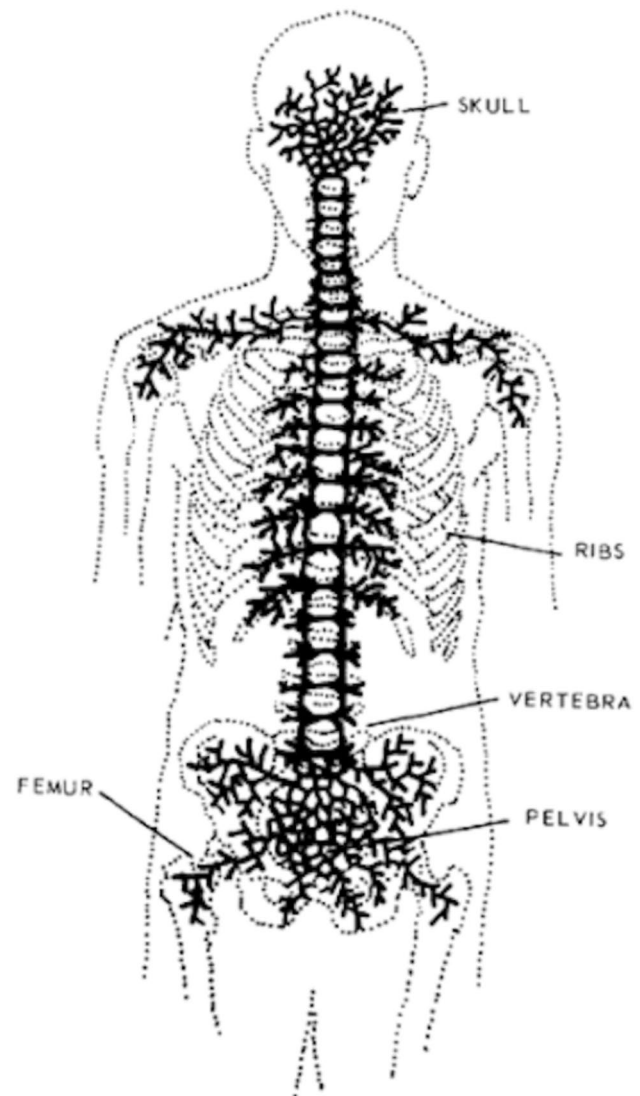


Fig. 1 Batson's venous plexus. Cited from *Diseases of the Spine and Spinal Cord* (Thomas N Byrne et al. P169, Oxford University Press)

the metabolic reaction of bone during the disease process, whether neoplastic, traumatic or inflammatory [13, 19].

Although plain radiographs are highly specific, they have low sensitivity (44–50%) [13]. Because of limited contrast, medullary lesions are more difficult to detect in trabecular bone than in cortical bone [13, 18].

The sensitivity of CT for the diagnosis of bone metastases ranges from 71 to 100% [13, 20]. Bone destruction and sclerotic deposits are usually clearly shown, and any soft tissue extension of bone metastases can be easily visualized [13]. However, the ability to detect inter-trabecular spread remains controversial [21–24].

18F FDG-PET detects the presence of bone metastases by directly quantifying metabolic activity [7, 13].

Fig. 2 Sample case (a–g) and osteoblastic change (h). The figure presents a 69-year-old man with multiple bone metastases from prostate cancer. Serum PSA was 4.894 ng/mL. **a** Total spine T1W image. Multiple low-intensity areas are shown in the spine, including in the L1 and L5 (arrowheads). **b** Total spine STIR image. Multiple mild, high-intensity areas are shown in the spine, including in the L1 and L5 (white arrowheads). **c** Body coronal in-phase T1W image. Multiple low-intensity areas can be seen (arrowheads). **d** Body coronal out-of-phase T1W image. Multiple slight high-intensity areas are shown in the lumbar spine (arrowheads). **e** Axial $b = 1000$ of the DW image at the level of the pelvic bone. High-intensity areas are shown in the sacrum and left ilium (white arrowheads). **f** Coronal reconstructed DW image. This image is displayed as a black-and-white inverted image. Multiple high-intensity areas are shown in the spine, including in the L1 and L5 (arrowheads). **g** Fused image combining in-phase coronal T1W image with coronal reconstructed DW image. Multiple high-intensity areas are shown in the spine, including in the L1 and L5 (white arrowheads). CT was performed at approximately the same time and revealed osteoblastic metastases. **h** Sagittal reconstruction of the CT image. Multiple sclerotic lesions can be seen, including in the L1 and L5 (white arrowheads), which were correlated with the low-intensity area in the T1W image and the high-intensity area in DW image. The diagnosis was osteoblastic metastases

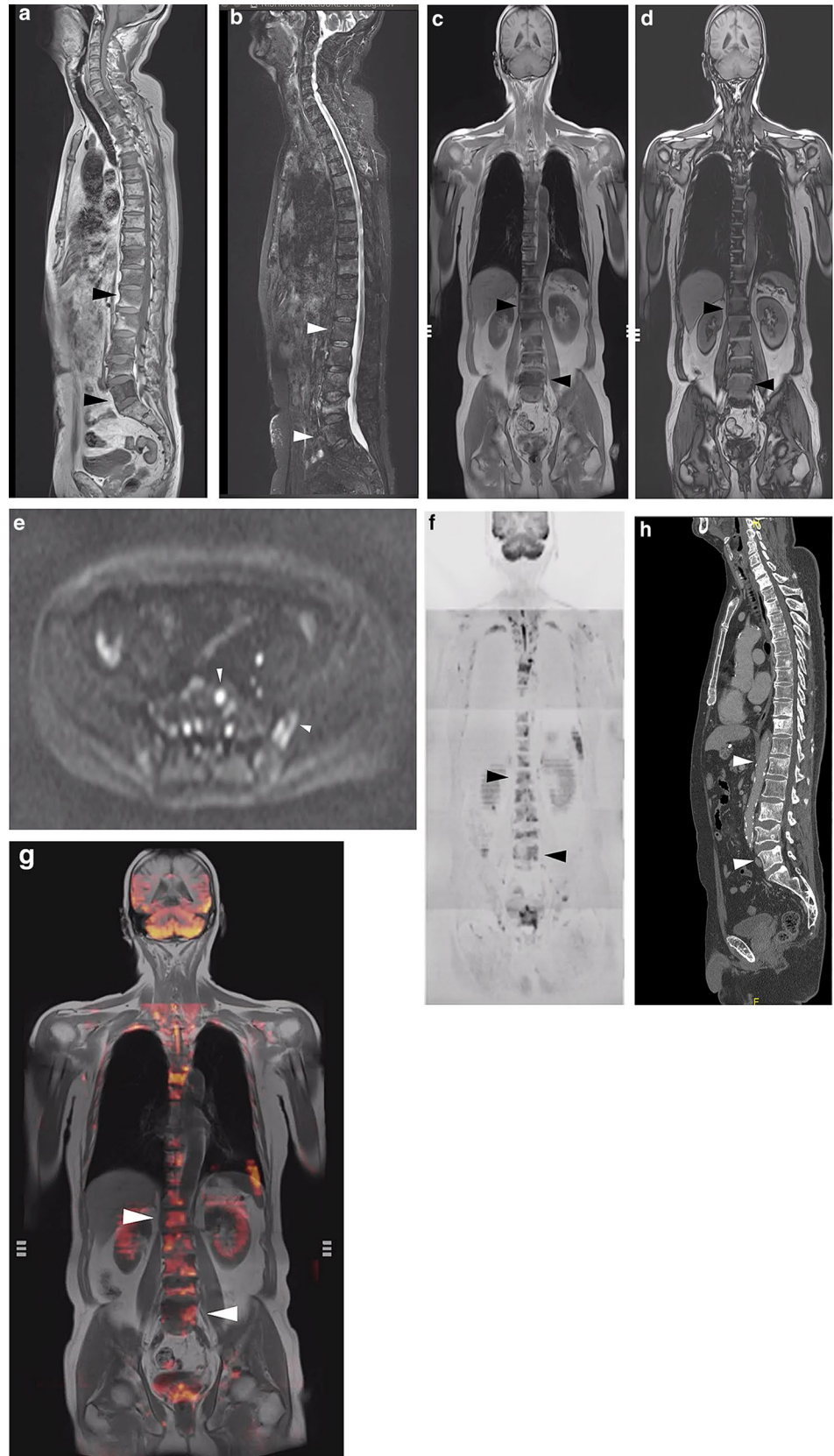




Fig. 3 Mixed-type/intertrabecular metastases. A 78-year-old man with a 4-year history of prostate cancer and transition to castration-resistant prostate cancer (CRPC). Serum PSA was 5.954 ng/mL. **a** On T1W image, multiple low-intensity areas are shown, including in the Th8 and Th11 (white arrowheads). **b** On the DW sagittal reconstructed image, multiple high-intensity areas are shown, including in

the Th8 and Th11 (arrowheads). **c** On the CT reconstructed sagittal image, obvious sclerotic or lytic changes were not observed. In fact, the diagnosis of multiple bone metastases using only CT examination was not possible. These CT findings were defined as intertrabecular metastases

MRI provides good contrast resolution of bone and soft tissue and therefore has good sensitivity and specificity for the detection for bone metastases [7, 9, 13]. However, limited field of view and long examination time pose problems, which existed even before the development of WB-MRI.

Traditionally, BS is the first choice for the diagnosis of bone metastases arising from prostate cancer. However, this method is considered insufficient, and a combination of CT and MRI is often used. Indeed, conventional modalities alone have been reported to be inadequate for the evaluation of treatment effects. [5, 25–27]. However, since the development of WB-MRI, the basis for diagnosing bone metastases from prostate cancer has changed.

Developmental history of WB-MRI

Reports comparing BS with MRI for the detection of bone metastases have been available since the last century [18]. However, our research has indicated that the oldest reports that included the term “whole-body MRI” date back to 1997 [28, 29]. Since the beginning in the twenty-first century, various devices have been developed to enable a whole-body scan in a single session without the need to change the directions of the body, which include multichannel coil and tabletop extenders [30–32].

In 2004, Takahara et al. [33] used DWI with background body signal suppression (DWIBS). Until the development of this method, DWI was predominantly used for investigations of the central nervous system, especially in cases of acute stroke [34]. However, several researchers have reported that

Name	ID	DOB
Physician	Exam date current	Exam date comparator

Soft tissues RECIST criteria	MET-RADS Prostate Report	Bones MET-RADS criteria																														
Primary Involved Y N RAC 1 ⁺ 2 ⁺ Comment		Skull Involved Y N RAC 1 ⁺ 2 ⁺ Comment																														
Pelvic nodes Involved Y N RAC 1 ⁺ 2 ⁺ Comment		Cervical spine Involved Y N RAC 1 ⁺ 2 ⁺ Comment																														
Retroperitoneal Involved Y N RAC 1 ⁺ 2 ⁺ Comment		Dorsal spine Involved Y N RAC 1 ⁺ 2 ⁺ Comment																														
Other nodes Involved Y N RAC 1 ⁺ 2 ⁺ Comment		Lumbosacral spine Involved Y N RAC 1 ⁺ 2 ⁺ Comment																														
Liver Involved Y N RAC 1 ⁺ 2 ⁺ Comment		Pelvis Involved Y N RAC 1 ⁺ 2 ⁺ Comment																														
Lungs Involved Y N RAC 1 ⁺ 2 ⁺ Comment		Thorax Involved Y N RAC 1 ⁺ 2 ⁺ Comment																														
Other sites Involved Y N RAC 1 ⁺ 2 ⁺ Comment	Limbs Involved Y N RAC 1 ⁺ 2 ⁺ Comment																															
OVERALL ASSESSMENT																																
	<table border="1" style="width:100%; border-collapse: collapse;"> <tr> <th>No dis</th> <th>CR</th> <th>PR</th> <th>SD</th> <th>PD</th> <th>Mixed</th> </tr> <tr> <td>Primary</td> <td></td> <td></td> <td></td> <td></td> <td>Minor or major</td> </tr> <tr> <td>Nodes</td> <td></td> <td></td> <td></td> <td></td> <td>for progressive lesions</td> </tr> <tr> <td>Viscera</td> <td></td> <td></td> <td></td> <td></td> <td>overall SD/PR</td> </tr> <tr> <td>Bones</td> <td></td> <td></td> <td>RAC 1/2</td> <td>RAC3</td> <td>RAC 4/5</td> </tr> </table>	No dis	CR	PR	SD	PD	Mixed	Primary					Minor or major	Nodes					for progressive lesions	Viscera					overall SD/PR	Bones			RAC 1/2	RAC3	RAC 4/5	
No dis	CR	PR	SD	PD	Mixed																											
Primary					Minor or major																											
Nodes					for progressive lesions																											
Viscera					overall SD/PR																											
Bones			RAC 1/2	RAC3	RAC 4/5																											
	Comments																															

Response assessment categories (RAC): 1 Response: highly likely; 2 Response: likely; 3 Stable; 4 Progression: likely; 5 progression: highly likely. Single lesion 1⁺ RAC only; ≥2 lesions or diffuse disease use both RACs

MTastasis Reporting and Data System for Prostate Cancer: Practical Guidelines for Acquisition, Interpretation, and Reporting [MET-RADS-P] of Whole-body MRI Evaluations of Multiorgan Involvement in Advanced Prostate Cancer. Eur Urol. 2017; 71:81-92

Radiologist	Date
--------------------	-------------

Fig. 4 MET-RADS-P template [65]. The MET-RADS-P template form allocates the presence of unequivocally identified disease to 14 predefined regions of the body



Fig. 5 Multichannel coil: 20-channel head coil, 32-channel spine coil, and two or three 18-channel body-array coils were combined to cover the area of Batson’s venous plexus, which is an area with a predilection for bone metastases

Table 1 Total Spine sagittal sequences

	T1WI fast SE	STIR
TR/TE/TI (ms)	520/8.8	5000/87/230
Echo train length	2	14
Slice thickness (mm)	4/4.4(gap)	4/4.4(gap)
FOV of each station (mm)	420	420
Matrix	320×240	320×240
No. of stations	3	3
Time of each station	1 min 1 s	1 min 28 s
Other	19 slices	19 slices

Table 2 Body coronal sequences

TR/TE (ms)	3.93/1.32(opposed phase), 2.45 (in-phase)
Slice thickness (mm)	4
FOV of each station (mm)	450
Matrix	416×312
No. of stations	3
Time of each station (s)	17 s
others	Breath hold scan, flip angle 10°

various malignancies in the body show similar high signal intensities [33, 35–37].

Takahara et al. adapted DWI for whole-body malignancy screening using free-breathing, short T1 inversion recovery, and a high-resolution three-dimensional display. They

Table 3 Axial DWI sequences

TR/TE/TI (ms)	6000/44/230
Slice thickness (mm)	5
FOV of each station (mm)	480
Matrix	256×192
No. of slices of each station	40
No. of stations	4 or 5
Time of each station	1 min 24 s
<i>b</i> value (mm ² /s)	0 and 1000

demonstrated that free-breathing scans work effectively and that short T1 inversion recovery enables excellent fat suppression, which suggested that the method could be a powerful screening tool for malignancies. In the field of WB-MRI, this paper was groundbreaking. Since then, numerous reports have been published on the addition of DWI to WB-MRI for the detection of bone metastases in not only prostate cancer, but also breast cancer, lung cancer, and multiple myeloma [5, 38–40]. Moreover, this led many researchers to pay more attention to the field of prostate cancer [6, 41–50].

There are numerous comparative studies on the use of BS with WB-MRI. However, because these studies relied on the use of various MR scanners and included various types of cases, the results are cross-sectional [25, 51–58]. However, in 2020, Sun et al. [27] performed a database search to conduct a meta-analysis to compare the diagnostic performance between WB-MRI and BS for the detection of bone metastases. The results showed that WB-MRI had higher but comparable patient-based specificity as BS (99% vs. 95%) but markedly higher sensitivity (94% vs. 80%). The authors concluded that WB-MRI has higher sensitivity and diagnostic accuracy than did BS and may be used for both the confirmation and exclusion of metastatic bone disease.

To date, many therapeutic agents have been developed [59–62], such as radium-223 dichloride [63] for castration-resistant prostate cancer (CRPC), which has a high occurrence of bone metastases [64]. With the increase in the number of treatment options and improvements in patient survival, the use of WB-MRI for providing accurate diagnosis and therapy monitoring has become crucial.

Since the mid-2010s, research has focused on the standardization [41–47] and therapy monitoring of WB-MRI [48].

Padhani et al. highlighted the need for expert recommendations for WB-MRI scans and developed the Metastasis Reporting and Data System for Prostate Cancer (MET-RADS-P) [41, 65]. An expert panel of the most experienced radiologists and nuclear medicine physicians in advanced prostate cancer imaging conducted a review [46] and formulated guidelines on the performance standards for WB-MRI for the assessment of multi-organ involvement in advanced prostate cancer (Fig. 4).

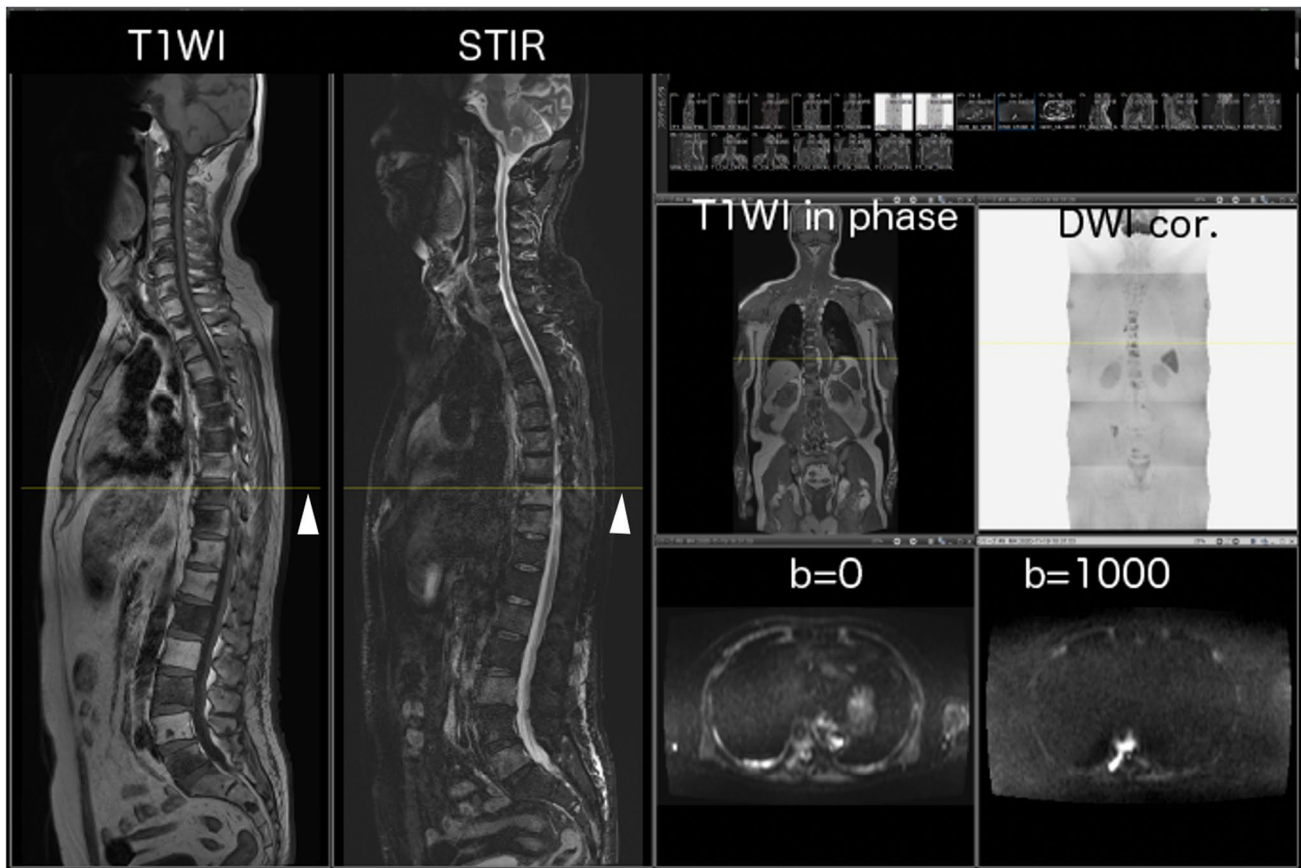


Fig. 6 Imaging layout. This image was captured using WB-MRI by the radiologists and comprised two monitors. On the left side of the monitor, the sagittal T1W images and STIR images are displayed by longitudinal two partings, and on the right side of the monitor, the

coronal in-phase T1W images, coronal reconstructed DW images, axial $b=0$, and axial $b=1000$ images were displayed by four partings. For all image planes, reference lines were used to detect the precise level of the regions (white arrowheads)

Padhani et al. [46] also reported the usefulness of WB-MRI for therapy monitoring. In addition, Padhani et al. suggested that WB-MRI provides a clear categorization of bone metastasis response and that the accurate assessment of therapy response would aid the rationale development of targeted therapies.

With progress of the standardization of WB-MRI and its use in therapy monitoring, there is now a need to quantify tumor volume and determine the apparent diffusion coefficient (ADC) value to enable precise evaluation of disease activity.

Blackledge et al. [66] reported the semi-automatic presentation of whole-body DWI for deriving tumor total diffusion volume (tDV) and associated global ADC.

This method is applicable for assessing treatment response in patients with bone metastases [47, 67–69]. Currently, the use of this device is favored for the precise evaluation of lesion detection and monitoring the therapeutic effect in patients with bone metastases.

Interpretation of imaging methods with WB-MRI

Recommended imaging methods and parameters

In this section, we show the representative imaging methods used in our department.

We used the Siemens Magnetom Prisma (3 T) scanner.

Multiple matrix coils covered patients from the lower neck to the proximal femur (Fig. 5), which also covered the Batson's venous plexus. Excluding the lower leg is controversial. In the trial by Lecouvet et al. [49], none of the patients had isolated peripheral metastases with WB-MRI, and only the axial-skeleton MRI in prostate cancer was missed.

The main examples of pulse sequences (Tables 1, 2, 3) and case (Fig. 2) are as follows:

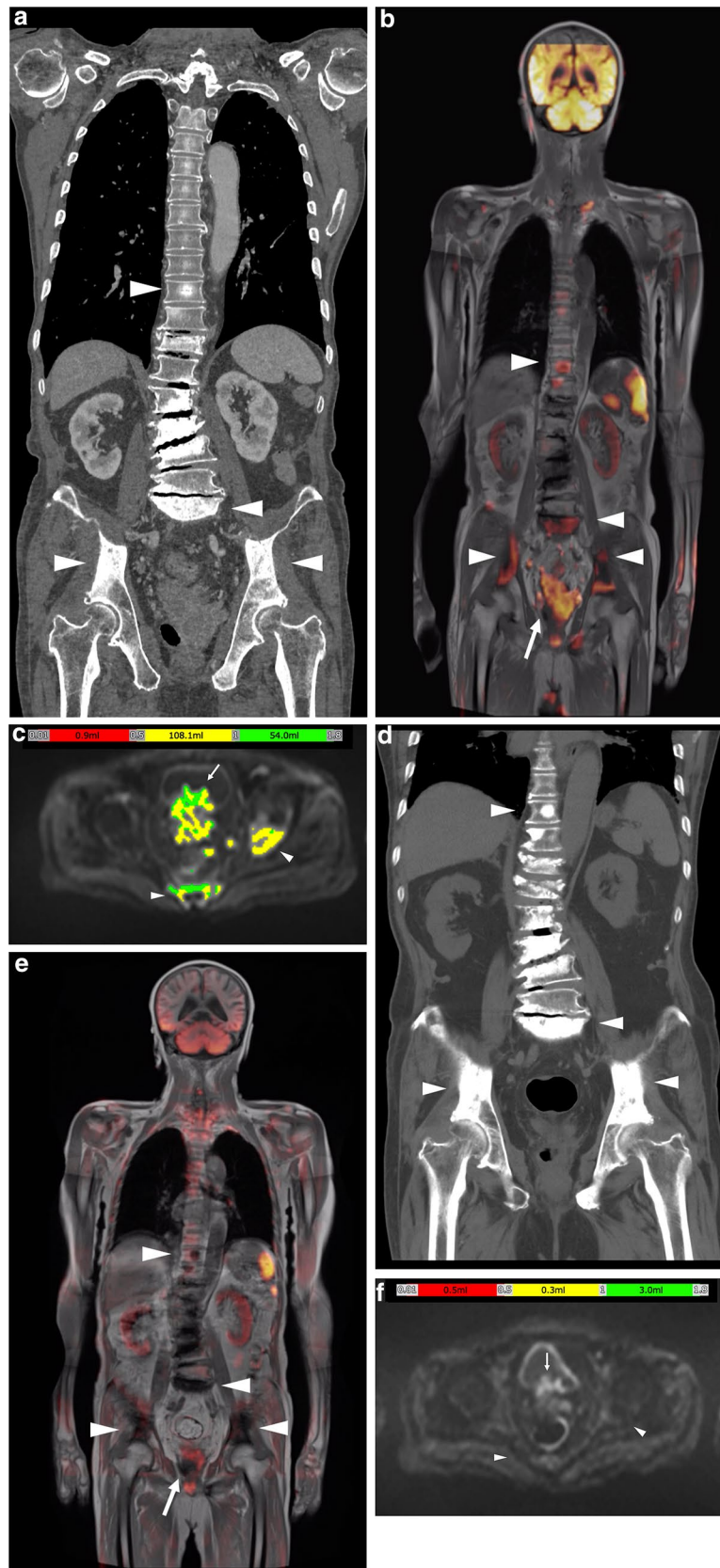


Fig. 7 An 85-year-old man who was initially diagnosed with primary unknown multiple bone metastases. **a** On the coronal reconstructed CT image, sclerotic lesions were observed in the bilateral ilium, sacrum and Th10 (white arrowheads), which were considered osteoblastic metastases. Sclerotic change in the lumbar spine appeared to be degenerative. Following the CT examination, a high serum PSA level (> 5000 ng/mL) was detected. **b** On the fused coronal DW and in-phase T1W image at a similar level to **a**, high-intensity areas were shown in the bilateral ilium, sacrum and Th10 (white arrowheads). In addition, the prostate gland was enlarged and appeared as high intensity (white arrow). **c** BD score composed axial image at the level of pelvis. The total volume of the area with a specific ADC value range (0.01 to 1.8×10^{-3} mm²/s in the image) is defined as tDV and is sub-categorized and denoted by a specific color (0.01–0.5: red, 0.5–1: yellow, 1–1.8: green). Color-displayed lesions are shown in the left acetabulum and sacrum (white arrowheads). The enlarged prostate gland can also be observed as color-displayed lesions (white arrow). In this case, the tDV was 163.0 mL, and the mean ADC of these lesions was calculated as $0.96 (\times 10^{-3}$ mm²/s) by the ADC histogram. **d–f**. Three months after the image shows in **a–c**, following combined androgen blockade. PSA decreased to 175.483 ng/mL. **d** On the coronal reconstructed CT, sclerotic change showed an increase from that in **a** in the bilateral ilium sacrum and Th10 (white arrowheads). **e** On the fused image, high-intensity areas in the bilateral ilium, sacrum, and Th10 decreased in intensity (white arrowheads), and the prostate gland decreased in size and intensity (white arrow) from those observed in **b**. **f** On the BD score-composed image, the color-displayed area shown in **c** largely disappeared (white arrowheads and white arrow). tDV markedly decreased to 3.8 mL, and mean ADC value increased to $1.18 (\times 10^{-3}$ mm²/s). Osteosclerotic change on **d** had been considered as the re-ossification after therapy

Total spine sagittal sequences

T1-weighted imaging (T1WI) and short T1 inversion recovery (STIR) consist of three stations (Table 1, Fig. 2a and b).

Body coronal sequences

Dixon's method consists of three stations (Table 2, Fig. 2c and d).

Axial diffusion-weighted sequences

Axial diffusion sequences are obtained with b value of 1000 (Fig. 2e) and 0, and the ADC map consists of four or five stations (Table 3).

The total examination time, including the positioning of the patient, is approximately 23 min.

After image acquisition, image processing is performed.

From the axial DWI images, coronal (Fig. 2f) and radial images are reconstructed and displayed as black-and-white reversed images. In-phase coronal T1WI- and DWI-coronal reconstructed images are fused, and the fusion images are reconstructed (Fig. 2g).

Environment for image interpretation

The size of the imaging data is enormous; therefore, the environment for image interpretation is important. In our department, two 324.9×432.2 mm monitors are used for viewing all station-combined sagittal and coronal direction images simultaneously. Three image planes should always be shown, equipped with a reference line (Fig. 6).

Tumor quantification

In our department, after obtaining approval from our ethics committee (No18117), we use BD score (PixSpace Inc.), which is the only clinical research tool available and is used only for retrospective analysis. This software was developed for automatically calculating tDV and mean ADC based on the ADC histogram generated using the DWI image and arbitrarily defining the threshold of the ADC value, which ranges from 0 to $3 (\times 10^{-3}$ mm²/s). We defined the threshold as $1.8 (\times 10^{-3}$ mm²/s), based on the evaluations of the effects of various treatment (66). From all voxel data of $b=0$ and $b=1000$ DWI, lesions in which the ADC value ranges from 0 to $1.8 (\times 10^{-3}$ mm²/s) are rapidly extracted. Then the BD score, which is composed of the axial (Fig. 7c) and coronal images, is generated. After that, extracted normal anatomical structures with corresponded ADC value, such as spleen, testis, spinal cord, intestine, etc., are manually removed. Consequently, total diffusion volume of the remaining lesion is defined as tDV and mean ADC value of the area is calculated. The software is particularly useful for processing multiple and large lesions, such as multiple metastatic lesions detected by whole-body DWI. Thus, it has been adopted for evaluating the therapeutic effect of whole-body metastatic lesions.

Presentations of some typical cases of bone metastases in prostate cancer

WB-MRI is useful not only for diagnosing the distribution and spread of bone metastases, but also for monitoring the therapeutic effect.

In this section, we presented several cases that compare CT findings.

1. Primary osteoblastic metastases (Fig. 2).

In general, osteoblastic-type metastases are frequently observed in prostate cancer in the initial stage. In this case, osteosclerotic change is evident on CT images and appears as low intensity on T1WI images and high intensity on DWI images.

2. Primary mixed-type metastases/inter-trabecular metastases (Fig. 3).

Other types, such as osteolytic and inter-trabecular types, are also detectable.

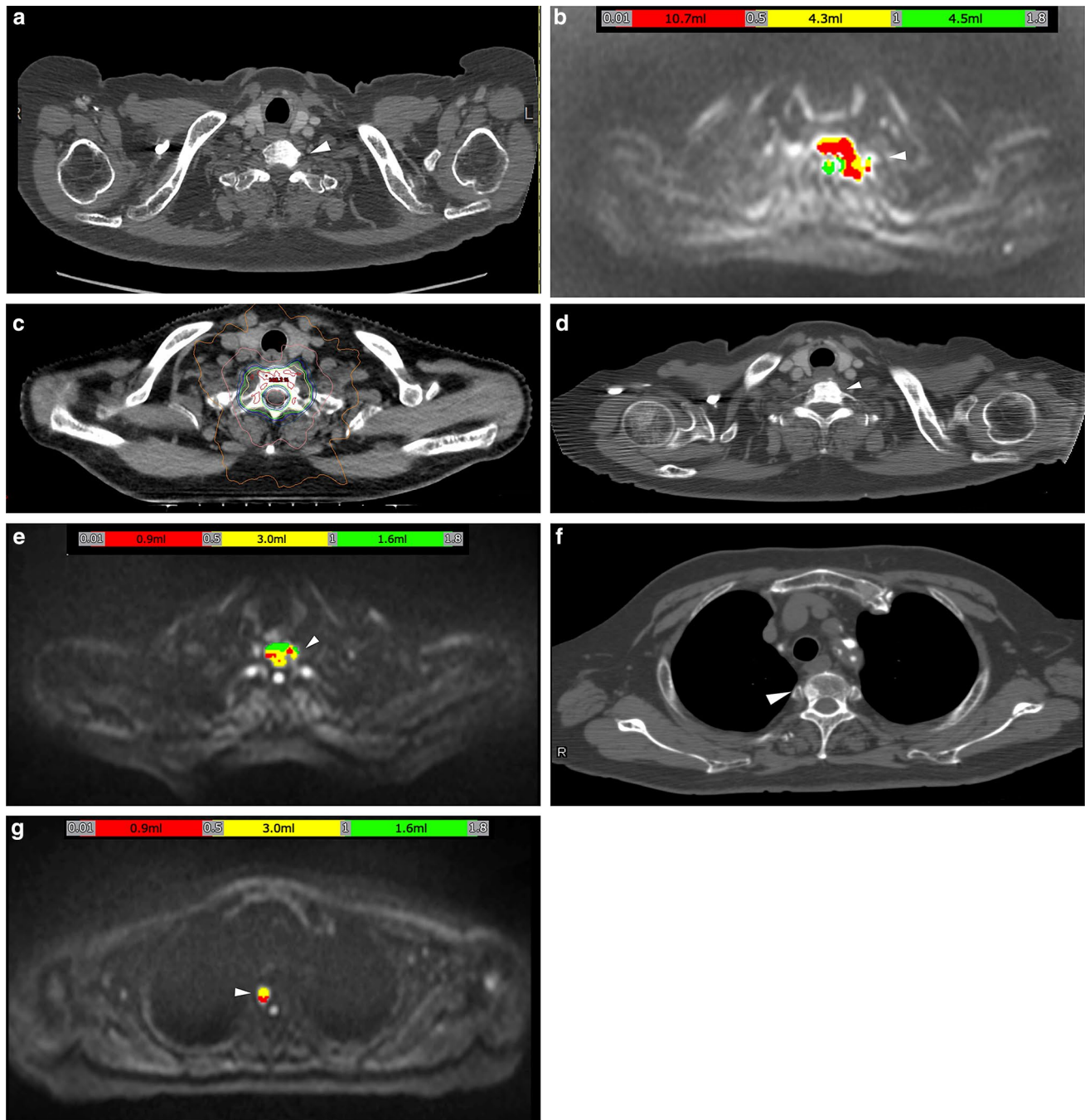


Fig. 8 A 70-year-old man with CRPC. Six years ago, local radiotherapy was performed for prostate cancer (T2c N0M0, PSA 32.1 ng/mL, GS 4+5). Four years later, the patient's condition transitioned to CRPC. **a** On the original axial CT at the level of C7, osteosclerotic change was seen in the left part of C7 body (white arrowhead). At that time, the patient's PSA level was 4.413 ng/mL. **b** On the BD score-composed axial image at the level of C7, a colored area was seen (white arrowhead). tDV was 19.5 mL, and the mean ADC value was $0.74 (\times 10^{-3} \text{ mm}^2/\text{s})$. **c** The C7 lesion was regarded a metastatic lesion, intensity-modulated radiation therapy was performed (35 Gy/5fr RT.) with reference to the axial DW image. **d–g** Approximately 10 months after the image shown in **a–c**, PSA increased

to 6.235 ng/mL. **d** On the original axial CT at the level of C7, the osteosclerotic change increased in the left part of the C7 body (white arrowhead) from that shown in **a**. **e** On the BD score-composed axial image at the level of C7, a colored area decreased from that in **b**. **f** On the CT image at the level of Th3, a subtle sclerotic change was newly observed (white arrowhead), but this was a retrospective finding. **g** On the BD score-composed axial image at the level of Th3, a colored area was newly observed in the right part of the body (white arrowhead). In this case, tDV decreased to 5.5 mL, and consequently, mean ADC increased to $0.83 (\times 10^{-3} \text{ mm}^2/\text{s})$; however, Th3 was diagnosed as a new metastatic lesion

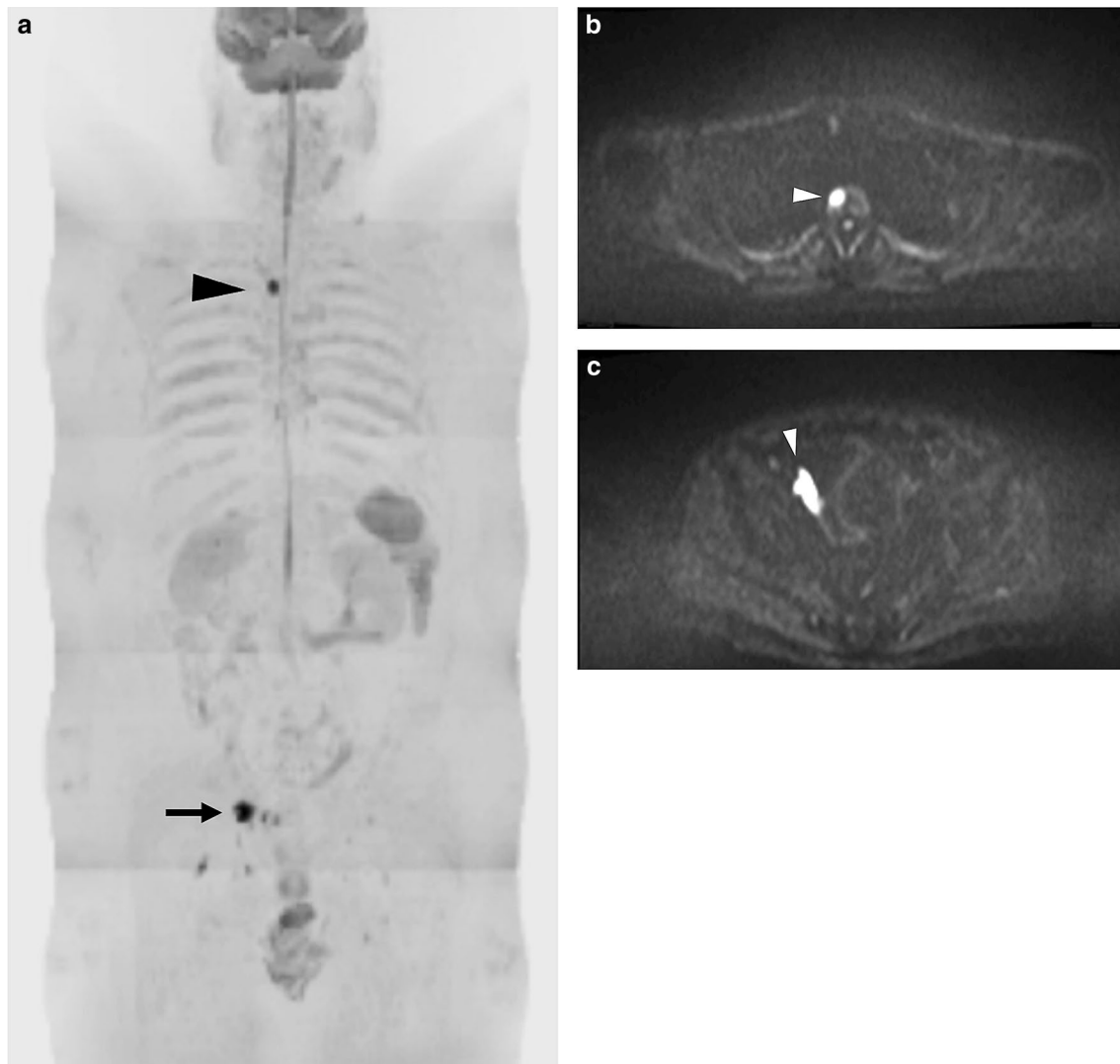


Fig. 9 Oligometastases. An 82-year-old man with bone metastases from prostate cancer. **a** On the radial reconstructed antero-posterior DW image, a high-intensity area was observed in Th2 (arrowhead), and swelling of the right internal iliac lymph node was suspected (arrow). At this time, the serum PSA was 34.903 ng/mL. **b** On the

$b = 1000$ axial DW image at the level of the Th2, a high-intensity area was seen (white arrowhead). **c** On the $b = 1000$ axial DW image at the level of the pelvis, the right iliac lymph node was swollen and had shown high intensity (white arrowhead)

In this case, CT images do not show the abnormal findings, such as bone formation or destruction, and DWI of MRI show high signal intensity.

3. Primary unknown osteoblastic metastases histologically confirmed as prostate cancer (Fig. 7).

During routine clinical experiences, we often encounter cases of osteoblastic metastases in men with an unknown primary site of origin, and prostate cancer is confirmed following initial radiological examinations. In such cases, multiple high-intensity areas are noted in WB-DWI images, and these are diagnosed as multiple bone metastases. In addition, the prostate gland is carefully observed on axial and coronal reconstructed DWI images. Predicting

the primary site before assessing for high serum PSA levels is sometimes possible.

4. Therapeutic effect of bone metastases (Figs. 7 and 8).

For monitoring the therapeutic effect, both therapy-reactive lesions and newly recurred lesions are often observed in the same case.

DWI enables precise evaluation of such lesions.

Radiologists should be aware that a CT finding of osteosclerotic change in metastatic lesions has two possibilities (Figs. 7 and 8). One of these is the osteoblastic metastasis itself (Fig. 7a and 8f), and the other is the re-ossification of the therapeutic effect (Fig. 7d and 8d). Several previous studies have reported the re-ossification of

bone metastases after radiotherapy [70, 71], which mainly describe the improvement in the stability of osteolytic metastases. However, careful differentiation from osteoblastic metastasis is important.

Differentiation on CT is often difficult, whereas DWI allows easy differentiation between these two conditions. The former shows high intensity, and the latter shows decreased signal intensity or tumor volume (Fig. 8b and e). Differentiating the two conditions using only conventional MRI sequence only or CT is difficult.

5. Oligometastases (Fig. 9).

The term “oligometastases” were conceived by Hellman and Weichselbaum in 1995 [72]. They described it as an intermediate state of distant spread, reflecting disease with a low, slow and late metastatic spreading capacity [73, 74]. The exact lesion number or volume is not defined, but the St Gallen Advanced Prostate Cancer Consensus Conference (APCCC) reached a consensus (85% of the panel) that the presence of three synchronous metastases (bone and/or lymph nodes) should be used to define oligo-metastatic prostate cancer [75–77]. Various reports have indicated that the accurate assessment of metastatic burden using radiologic and functional imaging technique is crucial [77]. However, conventional imaging modalities, which include CT findings, have low sensitivity in detecting small-volume disease and may underestimate disease burden [73]. Therefore, WB-MRI has been offered as a modality for effectively detecting oligo-metastases [74, 75, 78, 79].

Future evolution of WB-MRI

Use of artificial intelligence (AI)

AI has been mainly adopted to reduce scanning time [80].

Kidoh et al. [81] conducted a trial of deep learning-based noise reduction for brain MRI. In addition, Kashiwagi et al. [82] developed deep learning-based reconstruction for denoising brain, lumbar spine, and knee images, with the ultimate goal of shorting scanning time and reduce noise.

Zormpas-Petridis et al. [83] reported a method of using AI with WB-DWI. Their study aimed to improve the image quality of repeated acquisition (NEX) to one image and considerably reduce scanning times and found that image quality was improved and the acquisition time was reduced from 30 to 5 min.

In addition, they indicated that the automatic segmentation of lesions and the removal of normal structures are required for AI when the tDV and mean ADC are calculated.

Collaboration of modern radionuclide tracer

Recently, numerous researchers have reported the use of modern radiotracers such as ^{11}C -Choline [84, 85] ^{18}F -NAF [86, 87], and ^{68}Ga -PSMA-PET [88–91].

^{68}Ga -PSMA-PET has shown to be more accurate than WB-MRI in identifying distant metastases [88, 89]. It is particularly effective in cases where PSA is lower than 0.5 ng/ml [90, 91]. However, the advantage of WB-MRI is its absence of radiation exposure, cost-effectiveness, and examination repeatability. Thus, the combination of WB-MRI and these tracers might be the next trend in research.

Summary

WB-MRI has been established as the gold standard for detecting bone metastases from prostate cancer. It has the advantages of being able to detect lesions that are overlooked by conventional modalities, such as CT and BS. Moreover, because of its repeatability, it can be used to monitor therapeutic effects. In addition, further shortening of imaging time and automatic image processing will likely continue to progress.

Acknowledgements The authors would like to thank the radiological technologists especially the MR team of Osaka International Cancer Institute and also thanks Enago(www.enago.jp) for English language review.

Author contributions Corresponding author (K.N) and co-authors (J.T, Y.N, N.M, A.S, A.N, H.S and M.S) who belong to diagnostic department analyzed and discussed all imaging data in this manuscript. Co-author who belongs to radiation oncologic department (K.K) provided all the images of intensity-modulated radiation therapy (Fig. 8c). Co-authors who belong to urologic department (Y.Y, A.N and K.N) concerned entire treatment strategies in all cases in this manuscript. Co-author who belongs to orthopedic department (S.T) concerned the treatment strategies about bone metastases in all cases in this manuscript. Co-author who belongs to Osaka University School of Medicine (N.T) played a role of overall control of this review.

Funding There is no funding item about this paper.

Availability of data and material All cases were belonged to Osaka International Cancer Institute and in all cases, informed consents were acquired. All clinical and imaging data were belonged to Osaka International Cancer Institute.

Code availability Not applicable.

Declarations

Conflicts of interest No conflicts of interest.

Open Access This article is licensed under a Creative Commons Attribution 4.0 International License, which permits use, sharing, adaptation, distribution and reproduction in any medium or format, as long as you give appropriate credit to the original author(s) and the source, provide a link to the Creative Commons licence, and indicate if changes were made. The images or other third party material in this article are included in the article's Creative Commons licence, unless indicated otherwise in a credit line to the material. If material is not included in the article's Creative Commons licence and your intended use is not permitted by statutory regulation or exceeds the permitted use, you will need to obtain permission directly from the copyright holder. To view a copy of this licence, visit <http://creativecommons.org/licenses/by/4.0/>.

References

- Lee K, Park HY, Kim KW, Lee AJ, Yoon MA, Chae EJ, et al. Advances in whole body MRI for musculoskeletal imaging: Diffusion-weighted imaging. *J Clin Orthop Trauma*. 2019;10(4):680–6.
- Lecouvet FE, Whole-Body MR. Imaging: musculoskeletal applications. *Radiology*. 2016;279(2):345–65.
- Albano D, La Grutta L, Grassedonio E, Patti C, Lagalla R, Midiri M, et al. Pitfalls in whole body MRI with diffusion weighted imaging performed on patients with lymphoma: what radiologists should know. *Magn Reson Imaging*. 2016;34(7):922–31.
- Grover VP, Tognarelli JM, Crossey MM, Cox IJ, Taylor-Robinson SD, McPhail MJ. Magnetic resonance imaging: principles and techniques: lessons for clinicians. *J Clin Exp Hepatol*. 2015;5(3):246–55.
- Stecco A, Trisoglio A, Soligo E, Berardo S, Sukhovei L, Carriero A. Whole-body MRI with diffusion-weighted imaging in bone metastases: a narrative review. *Diagnostics (Basel)*. 2018;8:3.
- Eiber M, Holzzapfel K, Ganter C, Eppler K, Metz S, Geinitz H, et al. Whole-body MRI including diffusion-weighted imaging (DWI) for patients with recurring prostate cancer: technical feasibility and assessment of lesion conspicuity in DWI. *J Magn Reson Imaging*. 2011;33(5):1160–70.
- Shibata H, Kato S, Sekine I, Abe K, Araki N, Iguchi H, et al. Diagnosis and treatment of bone metastasis: comprehensive guideline of the Japanese Society of Medical Oncology, Japanese Orthopedic Association, Japanese Urological Association, and Japanese Society for Radiation Oncology. *ESMO Open*. 2016;1(2):e000037.
- Allemani C, Weir HK, Carreira H, Harewood R, Spika D, Wang XS, et al. Global surveillance of cancer survival 1995–2009: analysis of individual data for 25,676,887 patients from 279 population-based registries in 67 countries (CONCORD-2). *Lancet*. 2015;385(9972):977–1010.
- Migliorini F, Maffulli N, Trivellas A, Eschweiler J, Tingart M, Driessen A. Bone metastases: a comprehensive review of the literature. *Mol Biol Rep*. 2020;47(8):6337–45.
- Coleman RE. Clinical features of metastatic bone disease and risk of skeletal morbidity. *Clin Cancer Res*. 2006;12(20 Pt 2):6243s–s6249.
- Batson OV. The function of the vertebral veins and their role in the spread of metastases. *Ann Surg*. 1940;112(1):138–49.
- del Regato JA. Pathways of metastatic spread of malignant tumors. *Semin Oncol*. 1977;4(1):33–8.
- Macedo F, Ladeira K, Pinho F, Saraiva N, Bonito N, Pinto L, et al. Bone metastases: an overview. *Oncol Rev*. 2017;11(1):321.
- Yamaguchi T. Intertrabecular vertebral metastases: metastases only detectable on MR imaging. *Semin Musculoskelet Radiol*. 2001;5(2):171–5.
- Yamaguchi T, Tamai K, Yamato M, Honma K, Ueda Y, Saotome K. Intertrabecular pattern of tumors metastatic to bone. *Cancer*. 1996;78(7):1388–94.
- Fischer M, Kampen WU. Radionuclide therapy of bone metastases. *Breast Care (Basel)*. 2012;7(2):100–7.
- Keller ET, Zhang J, Cooper CR, Smith PC, McCauley LK, Pienta KJ, et al. Prostate carcinoma skeletal metastases: cross-talk between tumor and bone. *Cancer Metastasis Rev*. 2001;20(3–4):333–49.
- Algra PR, Bloem JL, Tissing H, Falke TH, Arndt JW, Verboom LJ. Detection of vertebral metastases: comparison between MR imaging and bone scintigraphy. *Radiographics*. 1991;11(2):219–32.
- Coleman R, Body JJ, Aapro M, Hadji P, Herrstedt J. Bone health in cancer patients: ESMO Clinical Practice Guidelines. *Ann Oncol*. 2014;25(Suppl 3):iii124–37.
- Rosenthal DI. Radiologic diagnosis of bone metastases. *Cancer*. 1997;80(8 Suppl):1595–607.
- Morita S, Suda T, Oda C, Kobayashi M, Hoshi T, Kanefuji T, et al. The value of (18)F-FDG PET in the diagnosis of intertrabecular vertebral metastasis in a small cell lung cancer patient with a high serum CEA level. *Intern Med*. 2019;58(3):415–8.
- Yoneyama S, Yumura Y, Koizumi M, Hanai T, Ishida H, Hattori Y, et al. A case of renal cell carcinoma with intertrabecular vertebral metastases detected F-18 fluorodeoxyglucose positron emission tomography and MRI. *Hinyokika Kyo*. 2014;60:29–32.
- Citrin DL. Problems and limitations of bone scanning with the 99Tcm-phosphates. *Clin Radiol*. 1977;28(1):97–105.
- McDougall IR, Kriss JP. Screening for bone metastases. Are only scans necessary? *JAMA*. 1975;231(1):46–50.
- Venkitaraman R, Cook GJ, Dearnaley DP, Parker CC, Khoo V, Eeles R, et al. Whole-body magnetic resonance imaging in the detection of skeletal metastases in patients with prostate cancer. *J Med Imaging Radiat Oncol*. 2009;53(3):241–7.
- Fujii Y, Higashi Y, Owada F, Okuno T, Mizuno H, Mizuno H. Magnetic resonance imaging for the diagnosis of prostate cancer metastatic to bone. *Br J Urol*. 1995;75(1):54–8.
- Sun G, Zhang YX, Liu F, Tu N. Whole-body magnetic resonance imaging is superior to skeletal scintigraphy for the detection of bone metastatic tumors: a meta-analysis. *Eur Rev Med Pharmacol Sci*. 2020;24(13):7240–52.
- Eustace S, Tello R, DeCarvalho V, Carey J, Wroblecka JT, Melhem ER, et al. A comparison of whole-body turboSTIR MR imaging and planar 99mTc-methylene diphosphonate scintigraphy in the examination of patients with suspected skeletal metastases. *AJR Am J Roentgenol*. 1997;169(6):1655–61.
- Chan Y, Chan K, Lam W, Metreweli C. Comparison of whole body MRI and radioisotope bone scintigram for skeletal metastases detection. *Chin Med J (Engl)*. 1997;110(6):485–9.
- Nakanishi K, Kobayashi M, Takahashi S, Nakata S, Kyakuno M, Nakaguchi K, et al. Whole body MRI for detecting metastatic bone tumor: comparison with bone scintigrams. *Magn Reson Med Sci*. 2005;4(1):11–7.
- Hargaden G, O'Connell M, Kavanagh E, Powell T, Ward R, Eustace S. Current concepts in whole-body imaging using turbo short tau inversion recovery MR imaging. *AJR Am J Roentgenol*. 2003;180(1):247–52.
- Lauenstein TC, Freudenberg LS, Goehde SC, Ruehm SG, Goyen M, Bosk S, et al. Whole-body MRI using a rolling table platform for the detection of bone metastases. *Eur Radiol*. 2002;12(8):2091–9.

33. Takahara T, Imai Y, Yamashita T, Yasuda S, Nasu S, Van Cauteren M. Diffusion weighted whole body imaging with background body signal suppression (DWIBS): technical improvement using free breathing, STIR and high resolution 3D display. *Radiat Med.* 2004;22(4):275–82.
34. Huisman TA. Diffusion-weighted imaging: basic concepts and application in cerebral stroke and head trauma. *Eur Radiol.* 2003;13(10):2283–97.
35. Ichikawa T, Araki T. Fast magnetic resonance imaging of liver. *Eur J Radiol.* 1999;29(3):186–210.
36. Guo Y, Cai YQ, Cai ZL, Gao YG, An NY, Ma L, et al. Differentiation of clinically benign and malignant breast lesions using diffusion-weighted imaging. *J Magn Reson Imaging.* 2002;16(2):172–8.
37. Kinoshita T, Yashiro N, Ihara N, Funatu H, Fukuma E, Narita M. Diffusion-weighted half-Fourier single-shot turbo spin echo imaging in breast tumors: differentiation of invasive ductal carcinoma from fibroadenoma. *J Comput Assist Tomogr.* 2002;26(6):1042–6.
38. Nakanishi K, Kobayashi M, Nakaguchi K, Kyakuno M, Hashimoto N, Onishi H, et al. Whole-body MRI for detecting metastatic bone tumor: diagnostic value of diffusion-weighted images. *Magn Reson Med Sci.* 2007;6(3):147–55.
39. Pearce T, Philip S, Brown J, Koh DM, Burn PR. Bone metastases from prostate, breast and multiple myeloma: differences in lesion conspicuity at short-tau inversion recovery and diffusion-weighted MRI. *Br J Radiol.* 2012;85(1016):1102–6.
40. Larbi A, Omoumi P, Pasoglou V, Michoux N, Triqueneaux P, Tombal B, et al. Whole-body MRI to assess bone involvement in prostate cancer and multiple myeloma: comparison of the diagnostic accuracies of the T1, short tau inversion recovery (STIR), and high b-values diffusion-weighted imaging (DWI) sequences. *Eur Radiol.* 2019;29(8):4503–13.
41. Padhani AR, Lecouvet FE, Tunariu N, Koh DM, De Keyzer F, Collins DJ, et al. METastasis reporting and data system for prostate cancer: practical guidelines for acquisition, interpretation, and reporting of whole-body magnetic resonance imaging-based evaluations of multiorgan involvement in advanced prostate cancer. *Eur Urol.* 2017;71(1):81–92.
42. Yoshida S, Takahara T, Arita Y, Ishii C, Uchida Y, Nakagawa K, et al. Progressive site-directed therapy for castration-resistant prostate cancer: localization of the progressive site as a prognostic factor. *Int J Radiat Oncol Biol Phys.* 2019;105(2):376–81.
43. Arita Y, Takahara T, Yoshida S, Kwee TC, Yajima S, Ishii C, et al. Quantitative assessment of bone metastasis in prostate cancer using synthetic magnetic resonance imaging. *Invest Radiol.* 2019;54(10):638–44.
44. Yoshida S, Takahara T, Ishii C, Arita Y, Waseda Y, Kijima T, et al. METastasis reporting and data system for prostate cancer as a prognostic imaging marker in castration-resistant prostate cancer. *Clin Genitourin Cancer.* 2020;18(4):e391–6.
45. Pricolo P, Ancona E, Summers P, Abreu-Gomez J, Alessi S, Jereczek-Fossa BA, et al. Whole-body magnetic resonance imaging (WB-MRI) reporting with the METastasis reporting and data system for prostate cancer (MET-RADS-P): inter-observer agreement between readers of different expertise levels. *Cancer Imaging.* 2020;20(1):77.
46. Padhani AR, Lecouvet FE, Tunariu N, Koh DM, De Keyzer F, Collins DJ, et al. Rationale for modernising imaging in advanced prostate cancer. *Eur Urol Focus.* 2017;3(2–3):223–39.
47. Perez-Lopez R, Mateo J, Mossop H, Blackledge MD, Collins DJ, Rata M, et al. Diffusion-weighted imaging as a treatment response biomarker for evaluating bone metastases in prostate cancer: a pilot study. *Radiology.* 2017;283(1):168–77.
48. Padhani AR, Makris A, Gall P, Collins DJ, Tunariu N, de Bono JS. Therapy monitoring of skeletal metastases with whole-body diffusion MRI. *J Magn Reson Imaging.* 2014;39(5):1049–78.
49. Lecouvet FE, Simon M, Tombal B, Jamart J, Vande Berg BC, Simoni P. Whole-body MRI (WB-MRI) versus axial skeleton MRI (AS-MRI) to detect and measure bone metastases in prostate cancer (PCa). *Eur Radiol.* 2010;20(12):2973–82.
50. Barchetti F, Stagnitti A, Megna V, Al Ansari N, Marini A, Musio D, et al. Unenhanced whole-body MRI versus PET-CT for the detection of prostate cancer metastases after primary treatment. *Eur Rev Med Pharmacol Sci.* 2016;20(18):3770–6.
51. Gutzeit A, Doert A, Froehlich JM, Eckhardt BP, Meili A, Scherr P, et al. Comparison of diffusion-weighted whole body MRI and skeletal scintigraphy for the detection of bone metastases in patients with prostate or breast carcinoma. *Skeletal Radiol.* 2010;39(4):333–43.
52. Wu Q, Yang R, Zhou F, Hu Y. Comparison of whole-body MRI and skeletal scintigraphy for detection of bone metastatic tumors: a meta-analysis. *Surg Oncol.* 2013;22(4):261–6.
53. Balliu E, Boada M, Peláez I, Vilanova JC, Barceló-Vidal C, Rubio A, et al. Comparative study of whole-body MRI and bone scintigraphy for the detection of bone metastases. *Clin Radiol.* 2010;65(12):989–96.
54. Sohaib SA, Cook G, Allen SD, Hughes M, Eisen T, Gore M. Comparison of whole-body MRI and bone scintigraphy in the detection of bone metastases in renal cancer. *Br J Radiol.* 2009;82(980):632–9.
55. Ketelsen D, Röthke M, Aschoff P, Merseburger AS, Lichy MP, Reimold M, et al. Detection of bone metastasis of prostate cancer - comparison of whole-body MRI and bone scintigraphy. *Rofo.* 2008;180(8):746–52.
56. Mentzel HJ, Kentouche K, Sauner D, Fleischmann C, Vogt S, Gottschild D, et al. Comparison of whole-body STIR-MRI and 99mTc-methylene-diphosphonate scintigraphy in children with suspected multifocal bone lesions. *Eur Radiol.* 2004;14(12):2297–302.
57. Pasoglou V, Larbi A, Collette L, Annet L, Jamar F, Machiels JP, et al. One-step TNM staging of high-risk prostate cancer using magnetic resonance imaging (MRI): toward an upfront simplified “all-in-one” imaging approach? *Prostate.* 2014;74(5):469–77.
58. Lecouvet FE, El Mouedden J, Collette L, Coche E, Danse E, Jamar F, et al. Can whole-body magnetic resonance imaging with diffusion-weighted imaging replace Tc 99m bone scanning and computed tomography for single-step detection of metastases in patients with high-risk prostate cancer? *Eur Urol.* 2012;62(1):68–75.
59. Ryan CJ, Smith MR, de Bono JS, Molina A, Logothetis CJ, de Souza P, et al. Abiraterone in metastatic prostate cancer without previous chemotherapy. *N Engl J Med.* 2013;368(2):138–48.
60. Scher HI, Fizazi K, Saad F, Taplin ME, Sternberg CN, Miller K, et al. Increased survival with enzalutamide in prostate cancer after chemotherapy. *N Engl J Med.* 2012;367(13):1187–97.
61. Petrylak DP, Tangen CM, Hussain MH, Lara PN Jr, Jones JA, Taplin ME, et al. Docetaxel and estramustine compared with mitoxantrone and prednisone for advanced refractory prostate cancer. *N Engl J Med.* 2004;351(15):1513–20.
62. de Bono JS, Oudard S, Ozguroglu M, Hansen S, Machiels JP, Kocak I, et al. Prednisone plus cabazitaxel or mitoxantrone for metastatic castration-resistant prostate cancer progressing after docetaxel treatment: a randomised open-label trial. *Lancet.* 2010;376(9747):1147–54.
63. Lien LM, Tvedt B, Heinrich D. Treatment of castration-resistant prostate cancer and bone metastases with radium-223 dichloride. *Int J Urol Nurs.* 2015;9(1):3–13.

64. Bubendorf L, Schöpfer A, Wagner U, Sauter G, Moch H, Willi N, et al. Metastatic patterns of prostate cancer: an autopsy study of 1,589 patients. *Hum Pathol.* 2000;31(5):578–83.
65. Padhani ATN. Metastatic prostate cancer in practice—the MET-RADS-P imaging response system using whole-body MRI. *MAGNETOM Flash* 2017;(68)2:64–72.
66. Blackledge MD, Collins DJ, Tunariu N, Orton MR, Padhani AR, Leach MO, et al. Assessment of treatment response by total tumor volume and global apparent diffusion coefficient using diffusion-weighted MRI in patients with metastatic bone disease: a feasibility study. *PLoS One.* 2014;9(4):e91779.
67. Blackledge MD, Tunariu N, Orton MR, Padhani AR, Collins DJ, Leach MO, et al. Inter- and intra-observer repeatability of quantitative whole-body, diffusion-weighted imaging (WBDWI) in metastatic bone disease. *PLoS One.* 2016;11(4):e0153840.
68. Perez-Lopez R, Lorente D, Blackledge MD, Collins DJ, Mateo J, Bianchini D, et al. Volume of bone metastasis assessed with whole-body diffusion-weighted imaging is associated with overall survival in metastatic castration-resistant prostate cancer. *Radiology.* 2016;280(1):151–60.
69. Perez-Lopez R, Tunariu N, Padhani AR, Oyen WJG, Fanti S, Vargas HA, et al. Imaging diagnosis and follow-up of advanced prostate cancer: clinical perspectives and state of the art. *Radiology.* 2019;292(2):273–86.
70. Rief H, Bischof M, Bruckner T, Welzel T, Askoxylakis V, Rieken S, et al. The stability of osseous metastases of the spine in lung cancer—a retrospective analysis of 338 cases. *Radiat Oncol.* 2013;8(1):200.
71. Foerster R, Habermehl D, Bruckner T, Bostel T, Schlamp I, Welzel T, et al. Spinal bone metastases in gynecologic malignancies: a retrospective analysis of stability, prognostic factors and survival. *Radiat Oncol.* 2014;9:194.
72. Hellman S, Weichselbaum RR. Oligometastases. *J Clin Oncol.* 1995;13(1):8–10.
73. Palacios-Eito A, Béjar-Luque A, Rodríguez-Liñán M, García-Cabezas S. Oligometastases in prostate cancer: ablative treatment. *World J Clin Oncol.* 2019;10(2):38–51.
74. Nagahara A, Kanaki T, Yamamoto A, Yamamoto Y, Nakai Y, Nakayama M, et al. The efficacy of metastasis-directed radiation therapy (MDRT) for oligometastatic castration-resistant prostate cancer (CRPC). *J Clin Oncol.* 2020;38(6_suppl):240.
75. Larbi A, Dallaudière B, Pasoglou V, Padhani A, Michoux N, Vande Berg BC, et al. Whole body MRI (WB-MRI) assessment of metastatic spread in prostate cancer: therapeutic perspectives on targeted management of oligometastatic disease. *Prostate.* 2016;76(11):1024–33.
76. Gillessen S, Omlin A, Attard G, de Bono JS, Efstathiou E, Fizazi K, et al. Management of patients with advanced prostate cancer: recommendations of the St Gallen Advanced Prostate Cancer Consensus Conference (APCCC) 2015. *Ann Oncol.* 2015;26(8):1589–604.
77. Foster CC, Weichselbaum RR, Pitroda SP. Oligometastatic prostate cancer: reality or figment of imagination? *Cancer.* 2019;125(3):340–52.
78. Mottet N, van den Bergh RCN, Briers E, Van den Broeck T, Cumberbatch MG, De Santis M, et al. EAU-EANM-ESTRO-ESUR-SIOG Guidelines on Prostate Cancer-2020 update. Part 1: screening, diagnosis, and local treatment with curative intent. *Eur Urol.* 2021;79(2):243–62.
79. Ghafoor S, Burger IA, Vargas AH. Multimodality imaging of prostate cancer. *J Nucl Med.* 2019;60(10):1350–8.
80. Bhat CS, Chopra M, Andronikou S, Paul S, Wener-Fligner Z, Merkoulouvitich A, et al. Artificial intelligence for interpretation of segments of whole body MRI in CNO: pilot study comparing radiologists versus machine learning algorithm. *Pediatr Rheumatol Online J.* 2020;18(1):47.
81. Kidoh M, Shinoda K, Kitajima M, Isogawa K, Nambu M, Uetani H, et al. Deep learning based noise reduction for brain MR imaging: tests on phantoms and healthy volunteers. *Magn Reson Med Sci.* 2020;19(3):195–206.
82. Kashiwagi NTH, Yamashita Y, Miura A, Tanaka H, Kyotani K, et al. Feasibility of shortening the scanning time for spine MR images using deep learning-based noise reduction. In: 106th Annual meeting of Radiological Society of North America Chicago USA 2020.
83. Zormpas-Petridis KTN, Messiou C, Koh DM, Jamin Y, Blackledge M. Accelerating whole-body diffusion-weighted MRI with artificial intelligence. In: 105th annual meeting of radiological society of North America, Chicago USA 2019.
84. Wieder H, Beer AJ, Holzapfel K, Henninger M, Maurer T, Schwarzenboeck S, et al. 11C-choline PET/CT and whole-body MRI including diffusion-weighted imaging for patients with recurrent prostate cancer. *Oncotarget.* 2017;8(39):66516–27.
85. Eschmann SM, Pfannenbergs AC, Rieger A, Aschoff P, Müller M, Paulsen F, et al. Comparison of 11C-choline-PET/CT and whole body-MRI for staging of prostate cancer. *Nuklearmedizin.* 2007;46(5):161–8; quiz N47–8.
86. Sheikhabahaei S, Jones KM, Werner RA, Salas-Fragomeni RA, Marcus CV, Higuchi T, et al. (18)F-NaF-PET/CT for the detection of bone metastasis in prostate cancer: a meta-analysis of diagnostic accuracy studies. *Ann Nucl Med.* 2019;33(5):351–61.
87. Mosavi F, Johansson S, Sandberg DT, Turesson I, Sörensen J, Ahlström H. Whole-body diffusion-weighted MRI compared with (18)F-NaF PET/CT for detection of bone metastases in patients with high-risk prostate carcinoma. *AJR Am J Roentgenol.* 2012;199(5):1114–20.
88. Sawicki LM, Kirchner J, Buddensieck C, Antke C, Ullrich T, Schimmöller L, et al. Prospective comparison of whole-body MRI and (68)Ga-PSMA PET/CT for the detection of biochemical recurrence of prostate cancer after radical prostatectomy. *Eur J Nucl Med Mol Imaging.* 2019;46(7):1542–50.
89. Dyrberg E, Hendel HW, Huynh THV, Klausen TW, Løgager VB, Madsen C, et al. (68)Ga-PSMA-PET/CT in comparison with (18)F-fluoride-PET/CT and whole-body MRI for the detection of bone metastases in patients with prostate cancer: a prospective diagnostic accuracy study. *Eur Radiol.* 2019;29(3):1221–30.
90. Eiber M, Maurer T, Souvatzoglou M, Beer AJ, Ruffani A, Haller B, et al. Evaluation of hybrid ⁶⁸Ga-PSMA ligand PET/CT in 248 patients with biochemical recurrence after radical prostatectomy. *J Nucl Med.* 2015;56(5):668–74.
91. Petersen LJ, Nielsen JB, Dettmann K, Fisker RV, Haberkorn U, Stenholt L, et al. (68)Ga-PSMA PET/CT for the detection of bone metastasis in recurrent prostate cancer and a PSA level <2 ng/ml: Two case reports and a literature review. *Mol Clin Oncol.* 2017;7(1):67–72.

Publisher's Note Springer Nature remains neutral with regard to jurisdictional claims in published maps and institutional affiliations.

Authors and Affiliations

Katsuyuki Nakanishi¹ · Junichiro Tanaka¹ · Yasuhiro Nakaya¹ · Noboru Maeda¹ · Atsuhiko Sakamoto¹ · Akiko Nakayama¹ · Hiroki Satomura¹ · Mio Sakai¹ · Koji Konishi² · Yoshiyuki Yamamoto³ · Akira Nagahara³ · Kazuo Nishimura³ · Satoshi Takenaka⁴ · Noriyuki Tomiyama⁵

Junichiro Tanaka
junichiro.tanaka@oici.jp

Yasuhiro Nakaya
yasuhiro.nakaya@oici.jp

Noboru Maeda
maedano@mc.pref.osaka.jp

Atsuhiko Sakamoto
akkun205@gmail.com

Akiko Nakayama
akiko.nakayama@gmail.com

Hiroki Satomura
hiroki.satomura@gmail.com

Mio Sakai
mio.sakai@oici.jp

Koji Konishi
konisi-ko@mc.pref.osaka.jp

Yoshiyuki Yamamoto
yoshiyuki229@gmail.com

Akira Nagahara
akira.nagahara@oici.jp

Kazuo Nishimura
kazuo.nishimura@oici.jp

Satoshi Takenaka
s.takenaka.0816@gmail.com

Noriyuki Tomiyama
tomiyama@radiol.med.osaka-u.ac.jp

- ¹ Department of Diagnostic and Interventional Radiology, Osaka International Cancer Institute, 3-1-69 Otemae, Chuo-ku, Osaka 541-8567, Japan
- ² Department of Radiation Oncology, Osaka International Cancer Institute, 3-1-69, Otemae, Chuo-ku, Osaka 541-8567, Japan
- ³ Department of Urology, Osaka International Cancer Institute, 3-1-69, Otemae, Chuo-ku, Osaka 541-8567, Japan
- ⁴ Department of Orthopaedic Surgery, Osaka International Cancer Institute, 3-1-69, Otemae, Chuo-ku, Osaka 541-8567, Japan
- ⁵ Department of Diagnostic and Interventional Radiology, Osaka University Graduate School of Medicine, 2-2, Yamadaoka, Suita, Osaka, Suita 565-0871, Japan